Check for updates

Advanced Functional Materials

ADVANCED FUNCTIONAL MATERIALS
www.afm-journal.de

RESEARCH ARTICLE OPEN ACCESS

Twin Crystal Moiré Metasurfaces for Crossing Flat-Band Transport

Shida Fan[1] | Chenglin Han[1] | Kuan He[1] | Chadi Ellouzi[2] | Yunlong Wang[3] | Li-Qun Chen[4] | Jie Sun[3] | Zhaodong Xu[5,6] | Chen Shen[2] | Tianzhi Yang[1]

[1]School of Mechanical Engineering and Automation, Northeastern University, Shenyang, P. R. China | [2]Department of Mechanical Engineering, Rowan University, Glassboro, New Jersey, USA | [3]The State Key Laboratory of Digital Steel, Northeastern University, Shenyang, P. R. China | [4]School of Science, Harbin Institute of Technology, Shenzhen, P. R. China | [5]Institute of Dynamics and Smart Disaster Prevention, Northeastern University, Shenyang, P. R. China | [6]China-Pakistan Belt and Road Joint Laboratory on Smart Disaster Prevention of Major Infrastructures, Southeast University, Nanjing, P. R. China

Correspondence: Jie Sun (sunjie@ral.neu.edu.cn) | Zhaodong Xu (xuzhdgyq@seu.edu.cn) | Chen Shen (shenc@rowan.edu) | Tianzhi Yang (yangtianzhi@me.neu.edu.cn)

Received: 8 April 2026 | **Revised:** 22 May 2026 | **Accepted:** 28 May 2026

Keywords: acoustic magic angle | crossing flat band | dispersion curves | moiré lattice | twin

ABSTRACT

To date, the flat bands in magic-angle bilayer metasurfaces have been observed to remain inherently parallel and non-crossing in naturally occurring 2D materials. This limitation arises from the inherent in-plane symmetry of the lattice. Here, we introduce a twinning lattice in acoustic bilayer twisted moiré metasurfaces that is mirror symmetric with respect to the twin crystal boundary. This new degree of freedom modulates the asymmetric moiré dispersive behavior and helps to achieve distinct features that are not possible in conventional symmetric twisted moiré structures. By adjusting the twin crystal angle and bilayer twisting angle, it endows remarkably different dispersion characteristics separated by the twin boundary, such as dual hyperbolic, hyperbolic-flat band combinations or dual flat bands. Crucially, this transition is governed by a nontrivial topological invariant, the number of anti-crossing points N_{ACPS}, which dictates the global phase classification. In the dual flat band regime, the intersection at the twin boundary enables low-loss acoustic propagation with tunable directionality, serving as a distinct point for wave manipulation. By providing experimental validation of dispersion crossover at the twin crystal interface, this study paves the way for the design and development of twin acoustic moiré metasurfaces.

1 | Introduction

Metasurfaces, as emerging artificial materials with a thin profile, have attracted widespread attention in recent years due to their unique advantages in wave propagation control [1–3]. In particular, hyperbolic metasurfaces have become a research hotspot in optics, acoustics, and thermodynamics thanks to their distinctive hyperbolic dispersion characteristics [4–8], exhibiting wave control capabilities that surpass traditional materials. The concept of hyperbolic metasurfaces first appeared in photonic crystals, where the propagation of photons was controlled by tuning the dielectric constant and magnetic permeability [9, 10], or by adjusting the impedance of directional waveguides [11–15], thereby achieving extreme anisotropy and precise wave propagation control. Cao et al. [16]. achieved flat band superconductivity by twisting two layers of graphene at a "magic angle," thus opening the door to twisted electronics. Researchers have also introduced the moiré effect into hyperbolic metasurfaces, constructing bilayer moiré metasurfaces [17–27]. The moiré effect, through relative rotations between layers, creates different moiré patterns, providing more degrees of freedom to the hyperbolic metasurface and allowing more flexible control of wave

This is an open access article under the terms of the Creative Commons Attribution License, which permits use, distribution and reproduction in any medium, provided the original work is properly cited.
© 2026 The Author(s). *Advanced Functional Materials* published by Wiley-VCH GmbH

propagation properties [28–32]. The interlayer hybridization in bilayer metasurfaces has enabled significant progress in wave manipulation, including applications such as interlayer magnetism [33, 34]. Moiré hyperbolic metasurfaces combine the advantages of hyperbolic dispersion and the moiré effect, where the hybridization of bilayer dispersion curves can realize more complex dispersion relationships. Notably, by twisting at a specific angle, the dispersion curves can hybridize into flat bands [35–41], a phenomenon that occurs at the so-called magic angle. At this angle, moiré lattices enable low-loss propagation of electrons, photons, and phonons. Hu et al. [42]. achieved photon dispersion flat bands and low-loss propagation by twisting two α-MoO_3 metasurfaces; Yves et al. [43]. successfully realized dispersion flat bands on phonons by rotating two acoustic metasurfaces. Han et al. [44]. supplemented the theory and experiment and extended the bilayer structure to multilayer structures.

Despite significant progress in wave manipulation with moiré hyperbolic metasurfaces, bilayer moiré systems still face limitations. When the hybridized dispersion curves of the twisted bilayer metasurface form flat bands, the flat bands always remain parallel without intersection, and the waves propagate along a fixed direction. This is because the dispersion curves of the upper and lower layers of the bilayer metasurface exhibit orthogonal symmetry, preventing the hybridized flat bands from intersecting regardless of the degree of rotation. Such symmetry limits the versatility of engineering the dispersion characteristics of moiré structures.

To address this, we leverage the uniaxial mirror symmetry of twin crystals by breaking the in-plane axial symmetry. The incorporation of twin crystal structures in hyperbolic moiré metasurfaces provides an additional route for interface-level dispersion engineering. For example, Li et al. [45]. proposed a spin-dependent photonic device based on twinning hyperbolic metamaterials, leveraging the twin crystal structure and the anisotropic properties of metamaterials. In this work, each layer of the twin crystal metasurface exhibits mirror symmetry with respect to the central twin crystal boundary. By rotating the relative twisting angle of the twin crystal moiré hyperbolic metasurfaces system (TMHMs), the proposed structure allows independent tailoring of the dispersion characteristics on both sides of the twin boundary, enabling flexible transitions among dual flat-band, hyperbolic–elliptic, flat-band–elliptic, and dual elliptic states. These states are not arbitrary but are topologically protected phases characterized by distinct values of the invariant N_{ACPS}. Moreover, it supports flexible engineering of the refraction angle at the twin crystal interface, including both positive and negative refraction. By combining different twin crystal angles and twisting angles, various refraction angles can be achieved. This work lays the foundation for future advancements in acoustic wave control, offering a versatile platform for designing metasurfaces with tailored dispersion properties.

2 | Results and Discussion

In previous studies, photonic flat bands are achieved by twisting two layers of α-MoO_3 shown in Figure 1a. The structure array is orthogonal, with $\gamma = 90°$. At specific twisting angles, the bilayer dispersion curves hybridize into flat bands in a fixed direction. Similarly, Han et al. realized all-angle flat bands in an acoustic system by introducing a skew angle in the unit cell. By varying the skew angles, the structure is no longer an orthogonal array, with $\gamma \neq 90°$. Moreover, the flat bands can be in any direction, as illustrated in the lower part of Figure 1b, where the blue and orange dashed lines represent the transformed flat bands corresponding to the rotation angles θ_1 and θ_2, respectively. However, in both cases, while the transition from directional to omnidirectional flat bands is achieved, the flat bands always maintain a parallel configuration and remain non-crossing. In this study, we introduce a moiré twin crystal metasurface, as shown in Figure 1c. The metasurface exhibits mirror symmetry about the twin boundary, marked by the black dashed line. The relative rotation between the layers leads to the formation of crossing flat bands. Notably, while the twin-crystal metasurface is geometrically realized through a twin-boundary arrangement, its functionality is coupling-mediated, and the twin boundary enables a single global twist angle to program distinct wave behaviors on the two sides of the interface. Unlike traditional parallel flat bands, where energy localization is rigidly fixed and cannot touch certain propagation angles, the crossing structure breaks this directional limitation through symmetry breaking at the twin boundary. This unique feature allows the system to bridge previously inaccessible angular gaps. By adjusting the rotation angle, we can flexibly tune the propagation modes to access these specific directions, enabling versatile mode configurations on both sides. Figure S1 shows the dispersion curves, illustrating the evolution from a single layer to a twisted bilayer structure, and from hyperbolic to the twin crystal metasurface.

Figure 2a schematically illustrates the structural configuration and dispersion features of the twin crystal moiré metasurface. The design comprises two stacked metasurfaces—Twin A (blue) and Twin B (orange)—arranged in the xy-plane and separated by a subwavelength gap of $h = 0.1a$, where a denotes the lattice constant. These two layers are twisted relative to each other by an angle θ about the central point of the system, giving rise to a geometricmoiré pattern. The mirror-symmetric twin boundary lies along the y-axis at the metasurface's center. A monochromatic sound source operating at $f = 2670$ Hz is positioned beneath the metasurface to excite wave propagation.

In fact, the frequency range over which this effect is applicable is closely linked to the hyperbolic dispersion range of the unit structure, with an effective bandwidth spanning from approximately 2457 to 2696 Hz. The formation of the flat band effect is highly dependent on the frequency characteristics. As the frequency shifts, the curvature of the hyperbolic dispersion curve also changes, and the resulting angle required for flat band formation needs to be adjusted accordingly. When the hybridized dispersion curve forms a flat band, the twisting angle is referred to as the "magic angle," under which acoustic waves exhibit low-loss propagation and enhanced localization. The dashed box on the right shows the concept model of the twin crystal, representing different twin crystal angles β.

The corresponding sound field pattern at the magic angle is presented in Figure 2b. Notably, unlike the straight-line trajectories typically observed in conventional moiré metasurfaces, the sound pressure distribution here exhibits mirror-symmetric pathways, a feature that arises from the crossing of the dispersion curves.

16163028, 0, Downloaded from https://advanced.onlinelibrary.wiley.com/doi/10.1002/adfm.76382 by Northeastern University, Wiley Online Library on [04/06/2026]. See the Terms and Conditions (https://onlinelibrary.wiley.com/terms-and-conditions) on Wiley Online Library for rules of use; OA articles are governed by the applicable Creative Commons License

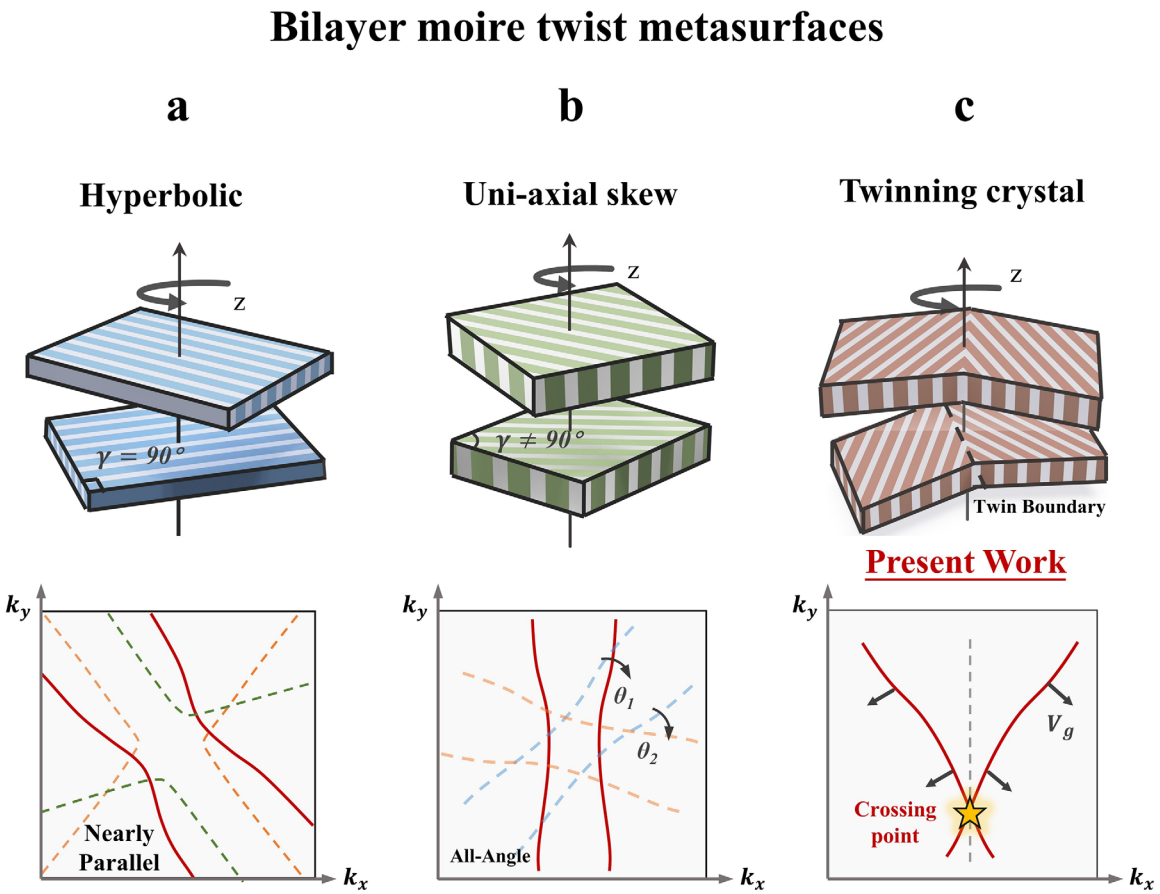

FIGURE 1 | Bilayer moiré twist metasurfaces. (a) Hyperbolic moiré metasurface: the array follows an orthogonal configuration, where the hybridization of the bilayers results in flat bands. In the lower plot, the red solid line represents the hybridized flat band, while the orange and green dashed lines indicate the dispersion curves of the upper and lower layers, respectively. (b) Uniaxially skewed hyperbolic moiré metasurface: the array is no longer orthogonal; by tuning the skew angles, flat bands can be realized in different directions, enabling flat bands with omnidirectional dispersion. (c) Twin crystal metasurface: this structure enables cross flat bands, with the intersection marked by the yellow pentagram in the lower plot.

The top-right corner shows the Fast Fourier Transform (FFT) of the sound pressure, the brightness distribution of the FFT clearly shows the dispersion characteristics in reciprocal space, providing an intuitive representation of the sound pressure propagation state. Traditional flat [46, 47] bands arise from intrinsic localized states within the system, where the group velocity is strictly zero, and energy is completely confined, unable to propagate. In contrast, the group velocity in our system approaches zero but does not vanish completely. This is because our flat band originates from the interlayer hybridization of dispersive hyperbolic modes (mediated by the air domain). Unlike static localization, this dynamic coupling mechanism inherently yields a quasi-flat dispersion with a finite slope, thereby supporting low-loss directional propagation rather than the complete energy stagnation associated with a perfect localized mode. In photonics, Hu. et al. [42]. achieved photonic quasi-flat bands by twisting α-MoO_3 bilayers, while in the elastic wave system, Li. et al. [30]. formed elastic wave flat bands by twisting anisotropic bilayers. These studies collectively validate that quasi-flat bands can be formed by anisotropic bilayer structures hybridized at the magic angle across different wave systems.

Figure 2c shows the sound pressure energy distribution along the propagation direction for the bilayer moiré twin crystal at the flat band and the single-layer Twin A. The plot depicts the variation of normalized energy as a function of propagation distance. The dispersion curve of the single-layer metasurface exhibits a hyperbolic shape, whereas the bilayer metasurface under flat band conditions shows a nearly linear dispersion curve, which reduces diffraction effects and enables low-loss propagation. To quantify energy loss, we define the energy loss factor as $\delta = (E_{max}\text{-}E_{min})/E_{max}$, where E_{max} and E_{min} represent the maximum and minimum normalized energy values, respectively. Over a propagation distance of five wavelengths, the flat band dispersion exhibits an energy loss factor of $\delta = 0.1$, whereas the hyperbolic dispersion has a significantly higher loss factor of $\delta = 0.61$. In elastic wave systems, a comparable trend has been reported, where the energy rapidly diminishes in the direction perpendicular to the flat-band propagation path, leading to a strong concentration near the center and pronounced attenuation toward the outer regions. These results indicate that in the single-layer twin crystal structure, sound pressure decays rapidly from the center toward the edges due to diffraction and energy leakage. Under the magic-angle flat-band condition of the bilayer twin crystal, the sound pressure remains nearly uniform along the propagation path, confirming the emergence of directionally guided and near-lossless acoustic transport—a hallmark

16163028, 0, Downloaded from https://advanced.onlinelibrary.wiley.com/doi/10.1002/adfm.76382 by Northeastern University, Wiley Online Library on [04/06/2026]. See the Terms and Conditions (https://onlinelibrary.wiley.com/terms-and-conditions) on Wiley Online Library for rules of use; OA articles are governed by the applicable Creative Commons License

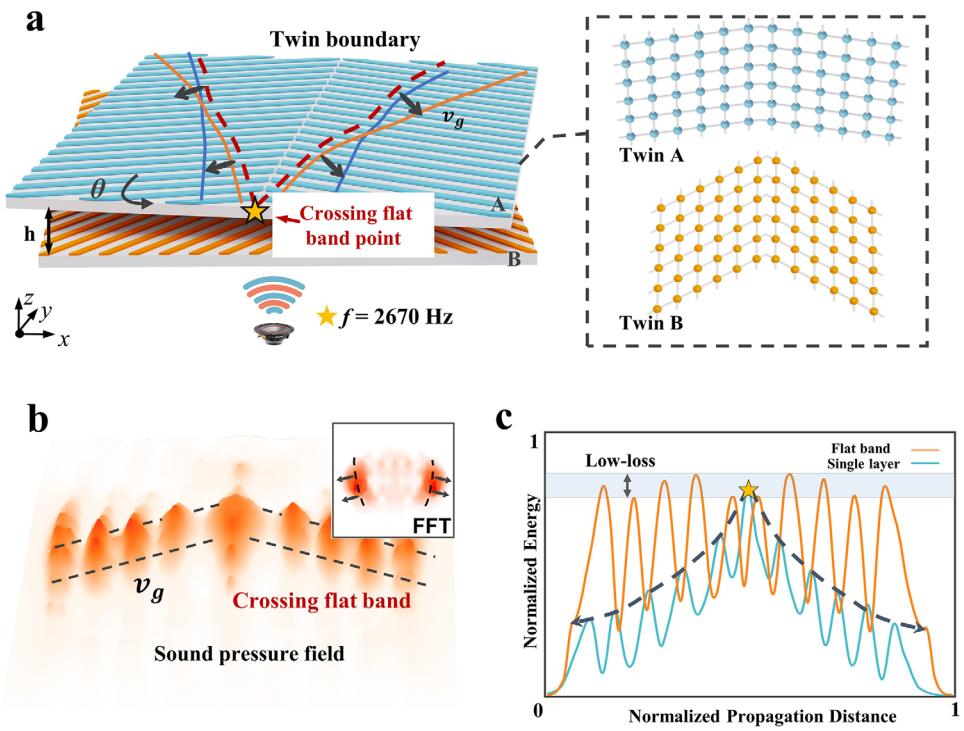

FIGURE 2 | Moiré twin crystal metasurface system. (a) Schematic diagram of the twin crystal twisting angles θ. The dispersion curves of Twin A and Twin B are represented by the blue and orange solid lines, respectively, with the red dashed line showing the hybridized dispersion curve, while the yellow pentagram marks their cross point; the system is excited by a point sound source, and the dashed box on the right illustrates the conceptual diagram of the upper and lower layers of the twin crystal. (b) Simulation of the sound pressure under the moiré twin crystal with dual flat bands, with the FFT of the sound pressure shown in the top-right corner. The black dashed line indicates the propagation direction of the sound field. (c) Sound pressure energy distribution for the bilayer Moiré twin crystal at the magic angle (orange line) and for the single-layer Twin A structure (blue line).

advantage of the proposed configuration over conventional designs.

To clearly illustrate the relationship between the rotation angle and different sound wave propagation modes, we present the angular relationships in both graphical and mathematical forms. These angles satisfy the following relations: $\alpha_1 = |\Delta\beta + \theta|$ and $\alpha_2 = |\Delta\beta — \theta|$, where $\Delta\beta$ represents the angle between β_1 and β_2. Figure 3a illustrates the angular relationship between Twin A and Twin B metasurfaces. The bilayer metasurface rotates around the center by an angle of θ. α_1 represents the difference in the twin crystal angles between the bilayer metasurface on the left side of the twin crystal boundary (the angle between the blue and green solid lines after the TMHMs rotation), α_2 denotes the angle on the right side of the twin crystal boundary. β_1 and β_2 denote the twin crystal angles for Twin A and Twin B, defined by the relative twist of the coupling tubes. These are explicitly marked in the bottom panel of Figure 3b, alongside the unit cell top views in the upper panels.

First, the intrinsic twin crystal angles, β_1 and β_2, are strategically determined to establish the geometric baseline. In the untwisted configuration ($\theta = 0^\circ$), we calibrate the effective alignment $\Delta\beta$ to strictly match the magic angle. Consequently, both α_1 and α_2 satisfy the critical condition, inducing flat bands on both sides of the interface to form a crossing flat-band configuration. This state supports symmetric low-loss channeling propagation across the twin boundary, as evidenced by the pressure field distribution in the upper-left panel of Figure 3d. Subsequently, by introducing a twist angle θ as a tuning parameter, α_1 and α_2 can be independently shifted into distinct topological regimes (hyperbolic, flat-band, or elliptical), thereby enabling arbitrary combinations of propagation modes on the two sides of the boundary. Moreover, the TMHMs exhibit remarkable robustness: as demonstrated in Section S4, even with the introduction of various defects, including point defects, line defects, translational misalignments, and random defects, the twin crystal metasurface demonstrates excellent robustness, with the acoustic fields remaining stable and intact.

The differences in propagation characteristics arise from the distinct effective coupling angles α_1 and α_2 on either side of the twin boundary. The system's magic angle is 21°, which corresponds to the critical contour-matching condition of the rotated hyperbolic isofrequency curves at the operating frequency. When the effective coupling angle is below, equal to, or above 21°, the hybridized contour remains hyperbolic, becomes nearly flattened for low-diffraction flat-band transport, or evolves into an elliptical propagation regime, respectively. The corresponding relationship between θ and α_1, α_2 is illustrated in Figure 3c. As Twin B rotates counterclockwise and θ increases, α_1 continuously increases, α_2 first decreases and then increases. Specifically, for the configurations discussed, when $\theta = 17^\circ$ and $\Delta\beta = 21^\circ$, $\alpha_1 = 38^\circ$ (greater than 21°) and $\alpha_2 = 4^\circ$ (less than 21°). On the α_2 side, the acoustic equal-frequency line is open, allowing sound waves to exhibit hyperbolic propagation; on the α_1 side, the acoustic equal-frequency line is closed, enabling sound waves to propagate in all directions, resulting in strong diffraction and significant energy

16163028, 0, Downloaded from https://advanced.onlinelibrary.wiley.com/doi/10.1002/adfm.76382 by Northeastern University, Wiley Online Library on [04/06/2026]. See the Terms and Conditions (https://onlinelibrary.wiley.com/terms-and-conditions) on Wiley Online Library for rules of use; OA articles are governed by the applicable Creative Commons License

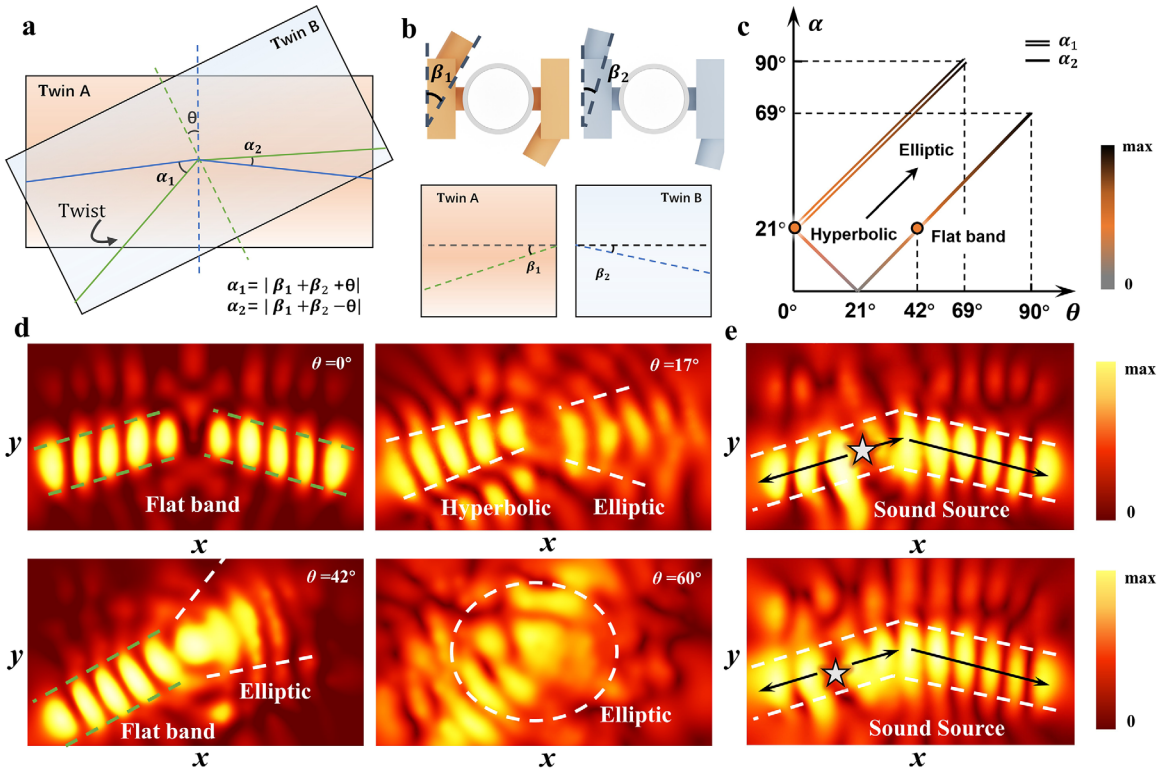

FIGURE 3 | Angle calculation and simulation observation of moiré Twin crystal metasurfaces. (a) Schematic diagram of angle calculation for moiré twin crystal metasurfaces. The upper and lower twin crystal layers rotate relative to each other by an angle θ, α_1, α_2 represent the angles between the unit cell array directions of Twin A and Twin B on the left side of the twin crystal boundary after the TMHMs rotation. (b) Schematic diagram of the unit cell structure of the two-layer twin crystal metasurface. (c) The relationship between the twist angle θ and α_1, α_2. For $\alpha < 21°$, the system exhibits hyperbolic propagation, whereas for $\alpha > 21°$, the hybridized dispersion curves close into an elliptic form. The double solid lines denote the variation of α_1, while the single solid line represents α_2. The orange circles indicate the parameter conditions for flat-band propagation. (d) Simulated sound pressure field diagrams at different rotation angles. (e) Acoustic negative refraction under off-center excitation. The top figure shows the sound source positioned two lattice constants to the left of the twin crystal interface; the bottom figure shows four lattice constants.

loss. When $\theta = 42°$, $\alpha_1 = 63°$ and $\alpha_2 = 21°$ ("magic angle"), one side of the system exhibits low-loss propagation, while the other side shows diffusive propagation. Similarly, when the twist angle is 60°, both sides exhibit elliptical divergent propagation. Figure 3d confirms through simulations the sound fields for all the above twisting angles. The three-dimensional view and FFT of the sound field are provided in Section S6. Additionally, we created a video illustrating the sound field propagation at different rotation angles, as detailed in Video S1.

This independent control enables key practical applications. For waveform filtering, the structure allows one side of the interface to support low-loss flat band propagation, while the other side can exhibit a divergent mode, enabling frequency-selective filtering. In waveguiding, adjusting the twin and rotation angles enables precise control of sound wave propagation, including special effects like negative refraction, offering flexibility in designing complex acoustic circuits and waveguides while preventing energy leakage.

This transition stems from a topological shift in the hybridized dispersion—from an open hyperbolic regime to a closed elliptic one—accompanied by a change in the number of anti-crossing points (N_{ACPS}) in the band structure. Here, N_{ACPS} is counted from the anti-crossing points of the hybridized isofrequency contours at the selected operating frequency. These anti-crossing points arise from the hybridization between the dispersion curves of the upper and lower layers and serve as a topological signature of the coupling evolution. It is noteworthy that the twin crystal metasurface enables the construction of different dispersion topologies on both sides of the "twin boundary." Specifically, it can realize combinations of flat band dispersion topologies, as well as hyperbolic or elliptical dispersion topologies on either side of the twin boundary. The values of N_{ACPS} (2 or 4) serve as a nontrivial topological invariant that fundamentally characterizes the global classification of the energy bands in the momentum space. The evolution from $N_{ACPS} = 2$ to $N_{ACPS} = 4$ marks a topological Lifshitz transition from hyperbolic to elliptical propagation. Supplementary Material Section 5 illustrates the variation of the hybridized dispersion bands and the evolution of the associated topological invariant with the twist angle.

However, the symmetric TMHMs are subject to strict topological constraints. The simultaneous realization of flat bands on both sides of the twin boundary is pinned to the untwisted state ($\theta = 0°$), where effective angles satisfy the magic condition symmetrically. Any non-zero twist ($\theta \neq 0°$) disrupts this balance, forcing the system into mixed dispersion regimes (e.g., hyperbolic-elliptical combinations) as governed by the angle-dependent evolution of N_{ACPS}. Consequently, to overcome this

16163028, 0, Downloaded from https://advanced.onlinelibrary.wiley.com/doi/10.1002/adfm.76382 by Northeastern University, Wiley Online Library on [04/06/2026]. See the Terms and Conditions (https://onlinelibrary.wiley.com/terms-and-conditions) on Wiley Online Library for rules of use; OA articles are governed by the applicable Creative Commons License

limitation and enable crossing flat bands at arbitrary intersection angles, an asymmetric design is required to compensate for the twist-induced deviation. To overcome this limitation, an asymmetric design can be further introduced so that the twinning angles on both sides of the twin boundary are no longer identical. This approach effectively breaks the mirror symmetry, enabling the formation of arbitrarily angled intersecting flat bands, thus offering greater flexibility and tunability in controlling acoustic wave propagation. More detailed discussions on this topic are provided in Section S7.

Remarkably, such an ability to engineer the propagation direction at the interface of the twin boundary endorses exceptional potential of TMHMs for refraction control. As acoustic waves pass across the twin boundary, their propagation direction is highly tunable based on the combined effects of the twin parameters and the twist angle θ. By properly designing these parameters, both conventional positive refraction and acoustic negative refraction effects can be achieved [48, 49]. In the case of negative refraction, the transmitted wave remains on the same side of the normal as the incident wave after crossing the twin boundary. Figure 3e shows simulation results with sound sources placed at different distances, both successfully demonstrating stable acoustic negative refraction. Notably, by adjusting both the twin crystal angle and the twist angle, the direction of the refracted wave can be finely tuned, granting the system tunable refraction angles. This capability significantly enhances the flexibility of acoustic wave control in moiré twin crystal metasurfaces, paving the way for novel applications in acoustic wave engineering and device design.

The prerequisite for achieving hyperbolic propagation with TMHMs is to determine the frequency range for hyperbolic propagation in the twin crystal structure. By scanning the Brillouin zone of the unit cell structure, its characteristic frequencies are obtained. These data can be used to plot the 3D dispersion curve of the structure, as shown in Figure 4a, its two-dimensional patterns and detailed information are provided in Section S2. This represents the dispersion curve of a single-layer structure, which is symmetric with respect to $k_x = 0$. Figure 4b intuitively illustrates the mirror-symmetric coupling tube structures on the left and right (orange and blue), which together form the twin crystal structure. This twin boundary interface is bridged by a twin boundary connector (Figure S13), a transitional link that maintains stable acoustic coupling through fixed mechanical constraints. The connector mainly adjusts the local coupling direction while preserving nearly unchanged channel cross-section, size, and effective air volume. The structures on both sides of the twin boundary are connected via non-local coupling, with the acoustic impedance of the coupling tubes exhibiting opposite imaginary components in the x and y directions, thus realizing hyperbolic dispersion. It is important to note that, in acoustic systems, wave propagation is confined within the air domain defined by the structure, where the air impedance is very low. Therefore, for most solid materials, the interface between air and solid can be considered an acoustically rigid boundary. As a result, the system's characteristics are primarily determined by the geometric structure and topological arrangement, with minimal dependence on the acoustic properties of the material itself.

According to the Bloch–Floquet theorem, the theoretical model is designed. For the single-layer unit cell structure, the symmetry of the dispersion curve matches that of the structure, both being mirror-symmetric with respect to the twin crystal boundary. To derive the dispersion relation of the unit cell, continuity conditions of normal mass velocity and sound pressure are imposed at three key locations along the vertical axis of the structure, corresponding to the upper, middle, and lower central points. The detailed theoretical formulation and boundary conditions are provided in Section S3.

$$P_{in} = P_{out} \tag{1}$$

$$V_{in} = V_{out} \tag{2}$$

Here, P_{in} and P_{out} represent the sound pressure of the incoming and outgoing sound waves, respectively; V_{in} and V_{out} represent the mass velocity of the incoming and outgoing sound waves. The dispersion equation can be obtained as follows

$$\begin{vmatrix} H_{11} - e^{ik_z d_h} & H_{12} \\ H_{21} & H_{22} - e^{ik_z d_h} \end{vmatrix} = 0 \tag{3}$$

In this equation, $\boldsymbol{H}$ represents a matrix, k_z is the z-component of the wavevector in air, and d_h is the height of the unit cell structure.

For the interlayer twisting in the bilayer structure, we introduce a rotation matrix, which allows us to obtain the theoretical dispersion curve. When the angular difference α_1 between the top and bottom layers of the TMHMs is 0°, the dispersion curves of the two layers hybridize as shown by the theoretical model in Figure 4c, and hyperbolic propagation is still observed. When the angular difference is changed to $\alpha_1 = 21°$, the hybridized dispersion curves transform into a flat band, with the theoretical model verified as shown in Figure 4d. At this point, sound wave transmission is non-diffractive, realizing low-loss propagation. The theoretical predictions agree well with the response of the TMHMs and capture the dispersion dynamics at different rotation angles.

To experimentally validate the twist-angle-dependent wave propagation predicted by our theoretical model, we fabricated the twin crystal metasurface using 3D printing, as shown in Figure 5a. An acoustic point source (diameter = 8 mm) was placed centrally beneath the metasurface for excitation. A reference sensor was positioned on one side, while another sensor performed automated scanning of the sound field on the opposite side. The entire setup was enclosed with perfectly matched layer material to suppress boundary reflections and external noise. Sound field measurements were conducted at various twist angles $\theta = 0°$, 17°, 42°, and 60°, with results shown in Figure 5c. At $\theta = 0°$, the measured field exhibits symmetric, low-loss propagation along the twin boundary, consistent with flat-band behavior. In contrast, at $\theta = 60°$, the sound field displays clear elliptic spreading, in excellent agreement with the simulated results in Figure 3d, with the measurements at $\theta = 17°$ and $\theta = 42°$ in excellent agreement with their corresponding simulations as well. These observations confirm that, although each 3D-printed layer has a fixed geometry after fabrication, distinct propagation regimes across the twin boundary can still be achieved by tuning the relative twist angle between the two layers, highlighting the

16163028, 0, Downloaded from https://advanced.onlinelibrary.wiley.com/doi/10.1002/adfm.76382 by Northeastern University, Wiley Online Library on [04/06/2026]. See the Terms and Conditions (https://onlinelibrary.wiley.com/terms-and-conditions) on Wiley Online Library for rules of use; OA articles are governed by the applicable Creative Commons License

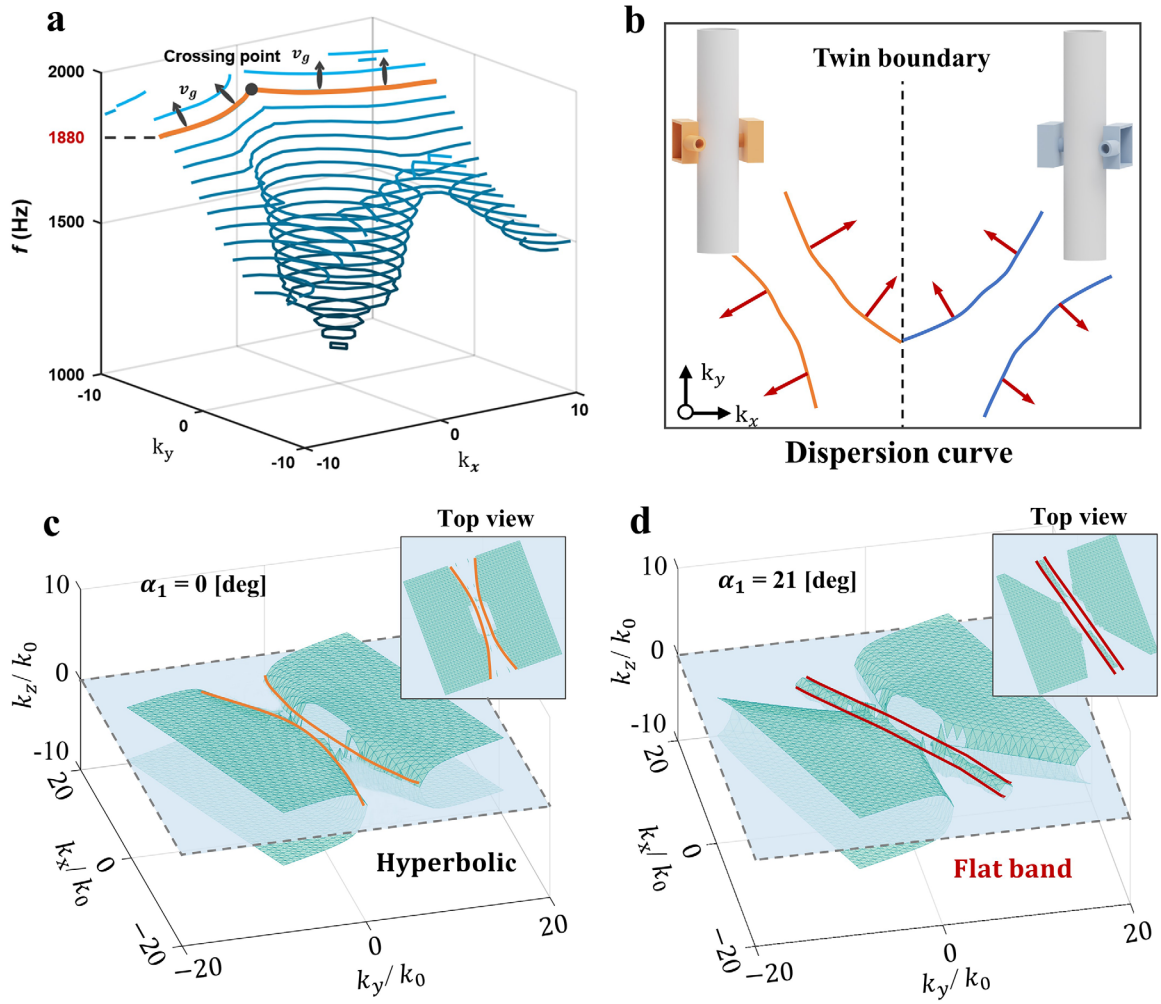

FIGURE 4 | The dispersion curve of TMHMs and the theoretical model. (a) Three-dimensional dispersion curve, with the orange curve representing the dispersion curve. At this frequency, the dispersion curve takes a hyperbolic shape and exhibits mirror symmetry about the center. The black arrows indicate the direction of the group velocity, which is perpendicular to the tangent direction. (b) The structures on both sides of the twin boundary and their corresponding dispersion curves, with the schematic diagrams of the respective structures shown in the top left and top right corners. (c) The three-dimensional theoretical model of the bilayer structure with $\alpha_1 = 0°$, in which the orange lines denote the hybridized dispersion curves, demonstrating typical hyperbolic propagation characteristics. The 3D top view of the model is displayed in the top right corner. (d) The theoretical model at $\alpha_1 = 21°$, the hybridized dispersion curve forms a flat band, with the red region indicating the corresponding flat band.

role of the twist-induced moiré effect in governing the hybridized dispersion through α_1 and α_2. For the experimental details of the asymmetric twin crystal metasurface, please refer to Section S8.

The interlayer coupling strength is directly controlled by the thickness of the air domain, h, which independently governs the intensity of the interlayer interaction. By controlling the thickness of the air domain between the two layers, it adjusts the intensity of the interlayer acoustic field interaction. For the twist angle, different twist angles lead to supercell structures with varying local geometric overlaps, resulting in different acoustic wave modes. As the twist angle changes, the interlayer geometric configuration is altered, which modulates the coupling characteristics. Our analysis indicates that the mode coupling is primarily governed by this local geometric overlap rather than strict parity selection rules. In this context, symmetry acts as a global constraint, defining the topological classification of the modes. Specifically, the structural symmetry and the twist angle enable flexible control over propagation modes, allowing arbitrary combinations on either side of the metasurface. A more detailed discussion on the coupling mechanism and geometric overlap is provided in Section S9.

At a twisting angle of $\theta = 0°$, we varied the coupling distance h between the two layers and measured the transmission rate of the sound waves passing through the metasurface. The relation between the transmission rate and coupling distance is shown in Figure 5b. The simulation results, represented by the green solid line and black circles, match perfectly with the experimental ones denoted by the blue diamonds. The results indicate that when $h < 1a$, the transmission rate drops rapidly, showing a strong coupling phenomenon. Conversely, when $h > 1a$, the rate of decrease in transmission is significantly lowered, indicating weak coupling. This phenomenon is clearly captured in the experimental results and agrees well with the simulations, as illustrated in Figure 5b. These experimental observations not only validate the theoretical

16163028, 0, Downloaded from https://advanced.onlinelibrary.wiley.com/doi/10.1002/adfm.76382 by Northeastern University, Wiley Online Library on [04/06/2026]. See the Terms and Conditions (https://onlinelibrary.wiley.com/terms-and-conditions) on Wiley Online Library for rules of use; OA articles are governed by the applicable Creative Commons License

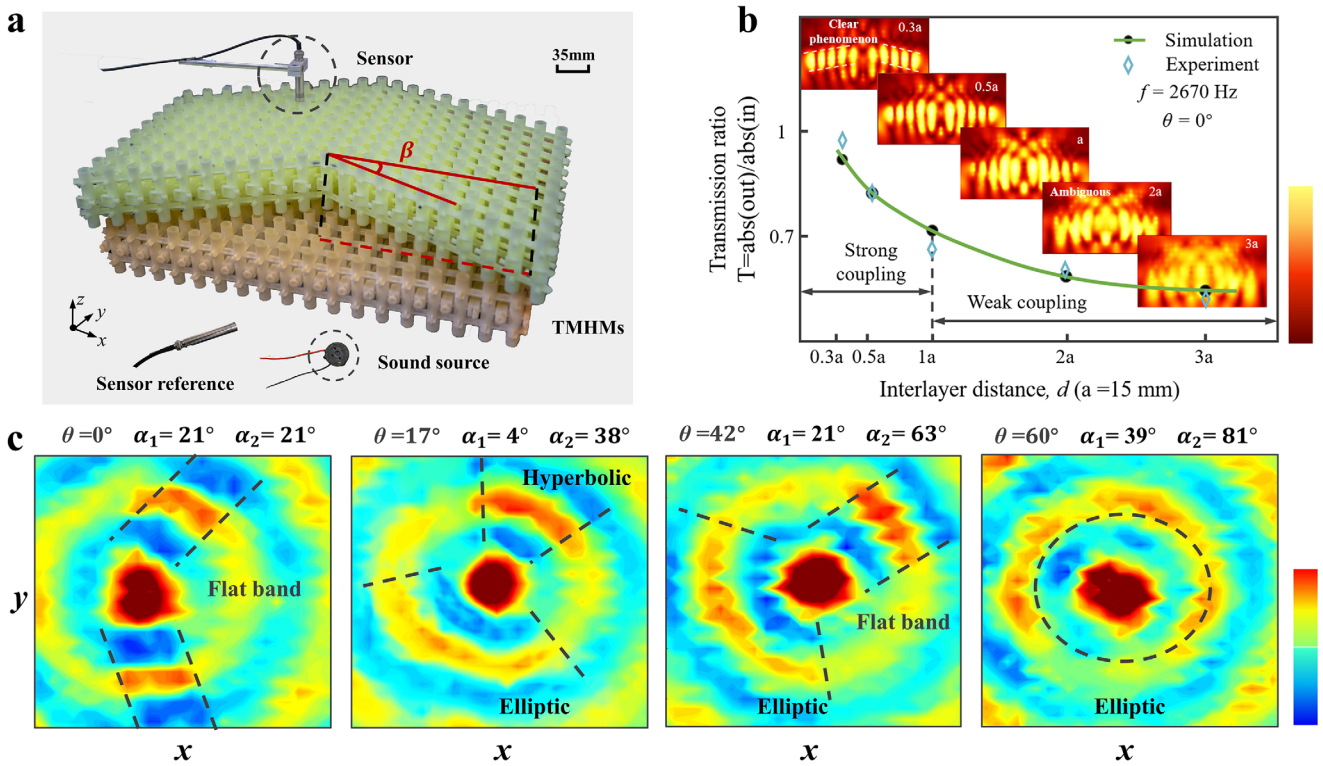

FIGURE 5 | Experimental measurements of the TMHMs at $f = 2670$ Hz. (a) Experimental setup for acoustic measurement. The moiré twin crystal metasurface was fabricated via 3D printing, with the sound source positioned beneath the structure for excitation, a reference probe placed below, and a scanning acoustic probe mounted above for field detection. (b) Impact of interlayer distance on the coupling effect in the TMHMs. The sound pressure field and sound pressure transmission rate were measured for different interlayer distances (0.3a, 0.5a, 1a, 2a, 3a). The green solid line with black circles represents the simulation results, the blue diamonds represent the experimental results. (c) Experimental measurement of the sound field distribution at different rotation angles ($\theta = 0°$, 17°, 42°, and 60°) in the TMHMs. The black dashed lines denote the direction of sound pressure propagation, demonstrating strong agreement between the experimental and simulated results.

model but also elucidate the combined influence of interlayer distance and rotational angle on modal behavior.

3 | Conclusion

Overall, this work demonstrates both theoretically and experimentally the flexible manipulation of acoustic waves using TMHMs. By tuning the twist angle θ, we achieved a variety of hybridized dispersion states across the twin boundary. Specifically, the two sides can simultaneously exhibit flat-band dispersion (enabling low-loss, channelized propagation), one side can support flat-band propagation while the other exhibits hyperbolic behavior, or both sides can enter hyperbolic or elliptic propagation regimes. Crucially, we established that these transitions are not arbitrary but are governed by a nontrivial topological invariant, N_{ACPS}. Moreover, by breaking the mirror symmetry—namely, by introducing asymmetric twinning angles on either side of the boundary—we enable arbitrarily angled intersections between flat bands, offering expanded control over mode localization and directionality. A theoretical model was developed that accurately captures the topological evolution of hybridized dispersion, including transitions in the number of anti-crossing points. We further explored the effect of interlayer spacing and found that when the separation exceeds one lattice constant, coupling weakens significantly and the field patterns become less pronounced—highlighting the importance of near-field interaction in TMHMs. Finally, acoustic field measurements exhibit excellent agreement with theoretical predictions, validating both the accuracy and reliability of the proposed model. These results not only deepen the understanding of moiré-induced topological acoustics but also offer new design principles for twist-programmed acoustic moiré devices, with promising applications in noise control, directional sound transport, and wave-based signal routing in mechanical systems.

Author Contributions

T.-Z.Y., C.S., L.-Q.C., and J.S. conceived the idea. S.-D.F., C.-L.H., and K.H. performed the experiments. S.-D.F., C.-L.H., C.E., and Y-L.W. carried out the theoretical analysis and simulations. S.-D.F. wrote the manuscript with contributions from the other authors. All of the authors have made a substantial contribution to the paper.

Acknowledgements

T.-Z.Y., S.-D.F., C.-L.H., and K.H. acknowledge support from the National Natural Science Foundation of China (Grant No. 12232014), the Natural Science Foundation of China (Grant No. 12072221), and the Ten Thousand Talents. All authors would like to thank Northeastern University, Rowan University, and Harbin Institute of Technology for their support of this study.

16163028, 0, Downloaded from https://advanced.onlinelibrary.wiley.com/doi/10.1002/adfm.76382 by Northeastern University, Wiley Online Library on [04/06/2026]. See the Terms and Conditions (https://onlinelibrary.wiley.com/terms-and-conditions) on Wiley Online Library for rules of use; OA articles are governed by the applicable Creative Commons License

Conflicts of Interest

The authors declare no conflicts of interest.

Data Availability Statement

The data that support the findings of this study are available from the corresponding author upon reasonable request.

References

1. Z. L. Li, P. Chen, K. Chen, et al., "Meta-Skin-Based Ultrasonic Instrument Enabling Highly Selective Ultrasound Stimulation and Treatment," *Advanced Devices & Instrumentation* 6 (2025): 0099, https://doi.org/10.34133/adi.0099.

2. L. S. Zeng, Z. B. Lin, Z. L. Li, et al., "High-Resolution Manifold Acoustic Holography Based on High-Pixel-Array Binary Metasurfaces," *Advanced Materials* 37 (2025): 2420229, https://doi.org/10.1002/adma.202420229.

3. Z. L. Li, L. X. Huang, Q. L. Sun, et al., "3D Acoustic Imaging Hitting the Diffraction Limit via Fully Parameter-Optimized Meta-Lens and Frequency-Domain Reconstruction," *Advanced Materials* 37 (2025): 08453, https://doi.org/10.1002/adma.202508453.

4. A. Aigner, J. M. Dawes, S. A. Maier, and H. Ren, "Nanophotonics Shines Light on Hyperbolic Metamaterials," *Light Science Applied* 11 (2022): 9, https://doi.org/10.1038/s41377-021-00688-2.

5. A. A. High, R. C. Devlin, A. Dibos, et al., "Visible-frequency Hyperbolic Metasurface," *Nature* 522 (2015): 192–196, https://doi.org/10.1038/nature14477.

6. G. Hu, W. Ma, D. Hu, et al., "Real-Space Nanoimaging of Hyperbolic Shear Polaritons in a Monoclinic Crystal," *Nature Nanotechnology* 18 (2023): 64–70, https://doi.org/10.1038/s41565-022-01264-4.

7. P. N. Li, I. Dolado, F. J. Alfaro-Mozaz, et al., "Infrared Hyperbolic Metasurface Based on Nanostructured van der Waals Materials," *Science* 359 (2018): 892–896, https://doi.org/10.1126/science.aaq1704.

8. Z. B. Zheng, F. S. Sun, W. C. Huang, et al., "Phonon Polaritons in Twisted Double-Layers of Hyperbolic van der Waals Crystals," *Nano Letters* 20 (2020): 5301, https://doi.org/10.1021/acs.nanolett.0c01627.

9. M. Luo, Y. Zhou, X. Zhao, et al., "High-Sensitivity Optical Sensors Empowered by Quasi-Bound States in the Continuum in a Hybrid Metal–Dielectric Metasurface," *ACS Nano* 18 (2024): 6477–6486, https://doi.org/10.1021/acsnano.3c11994.

10. S. You, M. Zhou, L. Xu, et al., "Quasi-Bound States in the Continuum with a Stable Resonance Wavelength in Dimer Dielectric Metasurfaces," *Nanophotonics* 12 (2023): 2051–2060, https://doi.org/10.1515/nanoph-2023-0166.

11. S. Huang, X. Fang, X. Wang, B. Assouar, Q. Cheng, and Y. Li, "Acoustic Perfect Absorbers via Helmholtz Resonators with Embedded Apertures," *The Journal of the Acoustical Society of America* 145 (2019): 254–262, https://doi.org/10.1121/1.5087128.

12. J. Li, W. Wang, Y. Xie, B.-I. Popa, and S. A. Cummer, "A Sound Absorbing Metasurface with Coupled Resonators," *Applied Physics Letters* 109 (2016): 091908, https://doi.org/10.1063/1.4961671.

13. G. Ma, M. Yang, S. Xiao, Z. Yang, and P. Sheng, "Acoustic Metasurface with Hybrid Resonances," *Nature Materials* 13 (2014): 873–878, https://doi.org/10.1038/nmat3994.

14. J. Mei and Y. Wu, "Controllable Transmission and Total Reflection through an Impedance-matched Acoustic Metasurface," *New Journal of Physics* 16 (2014): 123007, https://doi.org/10.1088/1367-2630/16/12/123007.

15. Z. Zhou, S. Huang, D. Li, J. Zhu, and Y. Li, "Broadband Impedance Modulation via Non-local Acoustic Metamaterials," *National Science Review* 9 (2022): nwab171, https://doi.org/10.1093/nsr/nwab171.

16. Y. Cao, V. Fatemi, S. Fang, et al., "Unconventional Superconductivity in Magic-Angle Graphene Superlattices," *Nature* 556 (2018): 43–50, https://doi.org/10.1038/nature26160.

17. J. Alvarez-Cuervo, M. Obst, S. Dixit, et al., "Unidirectional Ray Polaritons in Twisted Asymmetric Stacks," *Nature Communications* 15 (2024): 9042, https://doi.org/10.1038/s41467-024-52750-3.

18. D. Gromyko, S. An, S. Gorelik, et al., "Unidirectional Chiral Emission via Twisted Bi-layer Metasurfaces," *Nature Communications* 15 (2024): 9804, https://doi.org/10.1038/s41467-024-54262-6.

19. Y. Jin, W. Wang, Z. Wen, D. Torrent, and B. Djafari-Rouhani, "Topological States in Twisted Pillared Phononic Plates," *Extreme Mechanics Letters* 39 (2020): 100777, https://doi.org/10.1016/j.eml.2020.100777.

20. B. C. Lou, B. Wang, J. A. Rodríguez, M. Cappelli, and S. H. Fan, "Tunable Guided Resonance in Twisted Bilayer Photonic Crystal," *Science Advances* 8 (2022): add4339, https://doi.org/10.1126/sciadv.add4339.

21. M. J. Park, Y. Kim, G. Y. Cho, and S. Lee, "Higher-Order Topological Insulator in Twisted Bilayer Graphene," *Physical Review Letters* 123 (2019): 216803, https://doi.org/10.1103/PhysRevLett.123.216803.

22. N. C. Passler, X. Ni, G. Hu, et al., "Hyperbolic Shear Polaritons in Low-Symmetry Crystals," *Nature* 602 (2022): 595–600, https://doi.org/10.1038/s41586-021-04328-y.

23. L. Quan and A. Alù, "Hyperbolic Sound Propagation over Nonlocal Acoustic Metasurfaces," *Physical Review Letters* 123 (2019): 244303, https://doi.org/10.1103/PhysRevLett.123.244303.

24. E. M. Renzi, E. Galiffi, X. Ni, and A. Alù, "Hyperbolic Shear Metasurfaces," *Physical Review Letters* 132 (2024): 263803, https://doi.org/10.1103/PhysRevLett.132.263803.

25. X. Tan, B. Wang, S. Zhu, et al., "Novel Multidirectional Negative Stiffness Mechanical Metamaterials," *Smart Materials and Structures* 29 (2020): 015037, https://doi.org/10.1088/1361-665X/ab47d9.

26. P. Wang, Y. Zheng, X. Chen, et al., "Localization and Delocalization of Light in Photonic Moiré Lattices," *Nature* 577 (2020): 42–46, https://doi.org/10.1038/s41586-019-1851-6.

27. S. Yves, E. Galiffi, X. Ni, E. M. Renzi, and A. Alù, "Twist-Induced Hyperbolic Shear Metasurfaces," *Physical Review X* 14 (2024): 021031, https://doi.org/10.1103/PhysRevX.14.021031.

28. L. Bai, Y. Li, Y. L. Wang, J. Sun, and T. Z. Yang, "Nonlocal Mechanical Metamaterials Enabling Soliton Mode Conversion," *Small Structures* 6 (2025): 202500353, https://doi.org/10.1002/sstr.202500353.

29. J. Guan, J. T. Hu, Y. Wang, M. J. H. Tan, G. C. Schatz, and T. W. Odom, "Far-field Coupling between Moiré Photonic Lattices," *Nature Nanotechnology* 18 (2023): 514–520, https://doi.org/10.1038/s41565-023-01320-7.

30. M. H. Li, K. He, Z. W. Ren, et al., "Twist-on-Twist Moiré Elastic Metasurfaces," *Physical Review Letters* 135 (2025): 126301, https://doi.org/10.1103/qw7j-fj7b.

31. S. Liu, S. J. Ma, R. W. Shao, et al., "Moiré Metasurfaces for Dynamic Beamforming," *Science Advances* 8 (2022): abo1511, https://doi.org/10.1126/sciadv.abo1511.

32. L. Qu, W. Wu, D. Zhang, et al., "Beam Shaping by Stacked Nonlinear Moiré Metasurfaces," *Nano Letters* 25 (2025): 4854–4861, https://doi.org/10.1021/acs.nanolett.4c06570.

33. W. O. Chen, Z. Y. Sun, Z. J. Wang, et al., "Direct Observation of van der Waals Stacking–dependent Interlayer Magnetism," *Science* 366 (2019): 983–987, https://doi.org/10.1126/science.aav1937.

34. L. A. Gonzalez-Arraga, J. L. Lado, F. Guinea, and P. San-Jose, "Electrically Controllable Magnetism in Twisted Bilayer Graphene," *Physical Review Letters* 119 (2017): 107201, https://doi.org/10.1103/PhysRevLett.119.107201.

35. F. J. Culchac, R. R. Del Grande, R. B. Capaz, L. Chico, and E. S. Morell, "Flat Bands and Gaps in Twisted Double Bilayer Graphene," *Nanoscale* 12 (2020): 5014–5020, https://doi.org/10.1039/c9nr10830k.

36. J. Duan, G. Alvarez-Perez, C. Lanza, et al., "Multiple and Spectrally Robust Photonic Magic Angles in Reconfigurable α-MoO_3 Trilayers,"

16163028, 0, Downloaded from https://advanced.onlinelibrary.wiley.com/doi/10.1002/adfm.76382 by Northeastern University, Wiley Online Library on [04/06/2026]. See the Terms and Conditions (https://onlinelibrary.wiley.com/terms-and-conditions) on Wiley Online Library for rules of use; OA articles are governed by the applicable Creative Commons License

Nature Materials 22 (2023): 867–872, https://doi.org/10.1038/s41563-023-01582-5.

37. H. S. Ee and R. Agarwal, "Tunable Metasurface and Flat Optical Zoom Lens on a Stretchable Substrate," *Nano Letters* 16 (2016): 2818–2823, https://doi.org/10.1021/acs.nanolett.6b00618.

38. S. M. Gardezi, H. Pirie, S. Carr, W. Dorrell, and J. E. Hoffman, "Simulating Twistronics in Acoustic Metamaterials," *2D Mater* 8 (2021): 031002, https://doi.org/10.1088/2053-1583/abf252.

39. X. Liu, C. L. Chiu, J. Y. Lee, et al., "Spectroscopy of a Tunable Moiré System with a Correlated and Topological Flat Band," *Nature Communications* 12 (2021): 2732, https://doi.org/10.1038/s41467-021-23031-0.

40. M. M. Samak and O. R. Bilal, "Direct Observation of All-Flat Bands Phononic Metamaterials," *Physical Review Letters* 133 (2024): 266101, https://doi.org/10.1103/PhysRevLett.133.266101.

41. Z. Xu, X. Kong, J. Chang, D. F. Sievenpiper, and T. J. Cui, "Topological Flat Bands in Self-Complementary Plasmonic Metasurfaces," *Physical Review Letters* 129 (2022): 253001, https://doi.org/10.1103/PhysRevLett.129.253001.

42. G. W. Hu, Q. D. Ou, G. Y. Si, et al., "Topological Polaritons and Photonic Magic Angles in Twisted α-MoO_3 Bilayers," *Nature* 582 (2020): 209–213, https://doi.org/10.1038/s41586-020-2359-9.

43. S. Yves, Y.-G. Peng, and A. Alù, "Topological Lifshitz Transition in Twisted Hyperbolic Acoustic Metasurfaces," *Applied Physics Letters* 121 (2022): 122201, https://doi.org/10.1063/5.0107465.

44. C. Han, S. Fan, C. Li, L. Q. Chen, T. Yang, and C.-W. Qiu, "Nonlocal Acoustic Moiré Hyperbolic Metasurfaces," *Advanced Materials* 36 (2024): 2311350, https://doi.org/10.1002/adma.202311350.

45. Y. Li, J. Sun, Y. Wen, X. Xiong, L. Zhou, and J. Zhou, "Spin Photonics-Based on a Twinning Hyperbolic Metamaterial," *Advanced Functional Materials* 35 (2024): 2413351, https://doi.org/10.1002/adfm.202413351.

46. X. Zhang, T. Liu, Q. Zhang, X. Fan, F. Wu, and C. Qiu, "Observation of Ultraflat Bands in Gapped Moiré Metamaterials," *Physical Review B* 111 (2025): 125143, https://doi.org/10.1103/PhysRevB.111.125143.

47. K. C. Dong, T. C. Zhang, J. C. Li, et al., "Flat Bands in Magic-Angle Bilayer Photonic Crystals at Small Twists," *Physical Review Letters* 126 (2021): 223601, https://doi.org/10.1103/PhysRevLett.126.223601.

48. F. Gao, H. Xue, Z. Yang, et al., "Topologically Protected Refraction of Robust Kink States in Valley Photonic Crystals," *Nature Physics* 14 (2018): 140–144, https://doi.org/10.1038/nphys4304.

49. H. He, C. Qiu, L. Ye, et al., "Topological Negative Refraction of Surface Acoustic Waves in a Weyl Phononic Crystal," *Nature* 560 (2018): 61–64, https://doi.org/10.1038/s41586-018-0367-9.

Supporting Information

Additional supporting information can be found online in the Supporting Information section.

Supporting File 1: adfm76382-sup-0001-SuppMat.docx.

Supporting File 2: adfm76382-sup-0002-MoiveSI.mp4.

16163028, 0, Downloaded from https://advanced.onlinelibrary.wiley.com/doi/10.1002/adfm.76382 by Northeastern University, Wiley Online Library on [04/06/2026]. See the Terms and Conditions (https://onlinelibrary.wiley.com/terms-and-conditions) on Wiley Online Library for rules of use; OA articles are governed by the applicable Creative Commons License